Nanometer-scale temperature imaging for independent observation of Joule and Peltier effects in phase change memory devices

Kyle L. Grosse,[1] Eric Pop,[2] and William P. King[1,3,a)]
[1]*Department of Mechanical Science and Engineering, University of Illinois at Urbana-Champaign, Urbana, Illinois 61801, USA*
[2]*Department of Electrical Engineering, Stanford University, Stanford, California 94305, USA*
[3]*Departments of Electrical and Computer Engineering and Materials Science and Engineering, University of Illinois at Urbana-Champaign, Urbana, Illinois 61801, USA*

(Received 12 July 2014; accepted 2 September 2014; published online 19 September 2014)

This paper reports a technique for independent observation of nanometer-scale Joule heating and thermoelectric effects, using atomic force microscopy (AFM) based measurements of nanometer-scale temperature fields. When electrical current flows through nanoscale devices and contacts the temperature distribution is governed by both Joule and thermoelectric effects. When the device is driven by an electrical current that is both periodic and bipolar, the temperature rise due to the Joule effect is at a different harmonic than the temperature rise due to the Peltier effect. An AFM tip scanning over the device can simultaneously measure all of the relevant harmonic responses, such that the Joule effect and the Peltier effect can be independently measured. Here we demonstrate the efficacy of the technique by measuring Joule and Peltier effects in phase change memory devices. By comparing the observed temperature responses of these working devices, we measure the device thermopower, which is in the range of 30 ± 3 to 250 ± 10 μV K^{-1}. This technique could facilitate improved measurements of thermoelectric phenomena and properties at the nanometer-scale. [http://dx.doi.org/10.1063/1.4895715]

I. INTRODUCTION

Nanometer-scale Joule and thermoelectric effects dominate the temperature rise and energy consumption of electronic devices.[1] Optical thermometry techniques are commonly used to investigate Joule and thermoelectric effects in electronic materials,[2,3] but these techniques are diffraction limited to micrometer-scale resolution. Scanning probe microscopy (SPM) based techniques can achieve nanometer-scale resolution, but few studies have used SPM techniques to investigate Joule and thermoelectric effects in electronic devices. Recent work has used SPM based thermometry techniques to measure the local thermopower of graphene[4] and across GaAs *p-n* junctions[5] and has investigated Joule heating in Pt nanowires[6] and plasmonic devices.[7] However, these studies did not measure both Joule and thermoelectric effects in these devices at the nanometer-scale.

A few publications have reported the use of scanning Joule expansion microscopy (SJEM)[8] to investigate nanometer-scale Joule and thermoelectric effects.[9–11] SJEM is a frequency-domain thermometry technique that uses an atomic force microscopy (AFM) cantilever to measure the local thermo-mechanical expansions of a sample. SJEM operates by supplying a periodic voltage waveform to drive a device while the AFM measures the resulting thermo-mechanical expansions of the surface[10,12,13] and is capable of high spatial resolution (sub-50 nm) and temperature resolution (~200 mK).[9,11] Previous work has used the high spatial resolution of SJEM to study Joule and Peltier effects in carbon nanotubes (CNTs),[11] graphene,[9] and phase change memory (PCM) devices.[10] However, the coupled observation of Joule and Peltier effects yielded measurements with low sensitivity for observing nanometer-scale thermoelectric effects.

In this study, we developed the SJEM technique for independent observation of nanometer-scale Joule heating and thermoelectric effects, which increases the measurement sensitivity for observing thermoelectric effects at the nanometer-scale. Heating a device with a periodic and bipolar bias separates the temperature rise of the device due to Joule and thermoelectric effects at different harmonics. The separate observation of Joule and thermoelectric effects increases the sensitivity, throughput, and capabilities of the SJEM technique for observing thermoelectric effects at the nanometer-scale.

II. JOULE HEATING AND PELTIER EFFECTS

Figure 1(a) shows a two-terminal electronic device, where the device material has a thermopower $S > 0$. As current flows through the device, the temperature field near the contact interface is governed by both Joule heating (JH) and Peltier effects (PE). Figures 1(b) and 1(c) show the predicted temperature rise of the device due to PE and JH, and the supplementary material describes the finite element analysis (FEA) model used to predict the device temperature rise.[13]

Figure 1(b) shows the device temperature rise due to Peltier heating and cooling. For a positive thermopower material the Peltier effect locally heats (cools) the junction as carriers flow into (from) the metal contact.[9,10,14] Equation (1) describes heat generation due to PE as current flows from

a)Author to whom correspondence should be addressed. Electronic mail: wpk@illinois.edu

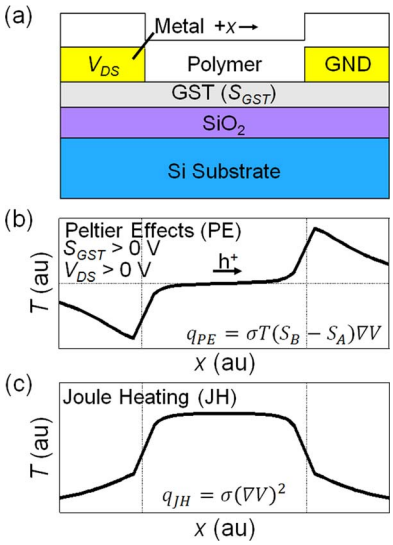

FIG. 1. Predicted device temperature rise T due to Joule heating (JH) and Peltier effects (PE). (a) Schematic of a $Ge_2Sb_2Te_5$ (GST) device with two electrodes. The left and right electrodes are biased at V_{DS} and 0 V. GST has a positive thermopower ($S_{GST} > 0$) and the electrodes have a low thermopower ($S \approx 0$). (b) Device temperature rise due to PE. The horizontal dashed line shows $T = 0$ K. (c) Device temperature rise due to JH.

material A to B.

$$q_{PE} = \sigma T(S_B - S_A)\nabla V, \tag{1}$$

where the material conductivity, absolute temperature, thermopower, and voltage are given by σ, T, S, and V.

Figure 1(c) shows the device temperature rise due to Joule heating. Joule heating is uniform and symmetric across the channel for a device with constant conductivity or resistivity. Joule heating also occurs at the contacts due to finite contact resistance between the channel and its contacts.[9] Equation (2) describes heat generation in a device due to JH.

$$q_{JH} = \sigma(\nabla V)^2. \tag{2}$$

The device temperature rise is a combination of Joule and Peltier effects, and a key observation is that Peltier effects scale with voltage and Joule heating scales with the voltage squared.

As periodic current flows through the device, the temperature field near the contact interface is governed by harmonic Joule and Peltier heating. Equation (3) describes the sinusoidal voltage waveform applied to the device.

$$V_{DS} = V_{0\omega} + V_{1\omega}\cos(2\pi\omega t), \tag{3}$$

where V_{DS}, ω, t, $V_{0\omega}$, and $V_{1\omega}$ are the device bias, frequency, time, zero harmonic (DC) voltage, and first harmonic voltage amplitude (a complex number). We define a bipolar waveform as a bias with no DC component ($V_{0\omega} = 0$ V) and a unipolar waveform as a bias with a single polarity ($|V_{0\omega}| = |V_{1\omega}|$). Applying a unipolar bias to a device is the current state-of-the-art for observing nanometer-scale Joule and Peltier effects.[9,10] Equations (4) and (5) describe Peltier and Joule heating of a device driven by a sinusoidal bias.

TABLE I. Voltage scaling of the temperature rise ΔT at the zero, first, and second harmonics (0ω, 1ω, and 2ω) due to JH and PE effects.

	Unipolar bias		Bipolar bias	
ΔT	JH	PE	JH	PE
0ω	$(V_{0\omega})^2 + 0.5(V_{1\omega})^2$	$V_{0\omega}$	$0.5(V_{1\omega})^2$	0
1ω	$2V_{0\omega} \times V_{1\omega}$	$V_{1\omega}$	0	$V_{1\omega}$
2ω	$0.5(V_{1\omega})^2$	0	$0.5(V_{1\omega})^2$	0

$$q_{PE} = \sigma T(S_B - S_A)[\nabla V_{0\omega} + \nabla V_{1\omega}\cos(2\pi\omega t)], \tag{4}$$

$$q_{JH} = \sigma[(\nabla V_{0\omega})^2 + 0.5(\nabla V_{1\omega})^2 + 2\nabla V_{0\omega}\nabla V_{1\omega}\cos(2\pi\omega t) + 0.5(\nabla V_{1\omega})^2\cos(2\pi 2\omega t)]. \tag{5}$$

Equations (4) and (5) were derived by substituting the device bias from Eq. (3) for the voltage V of Eqs. (1) and (2). Equations (4) and (5) describe heat generation in a device due to Joule and Peltier effects at the zero, first, and second harmonics (0ω, 1ω, and 2ω). A similar relation can be derived from Eq. (S5) of the supplementary material.[13]

Table I shows the voltage scaling of Joule and Peltier effects at the zero, first, and second harmonics due to bipolar and unipolar biases. Applying a unipolar bias causes JH to occur at all three harmonics and PE to occur at the zero and first harmonics. Unipolar heating causes JH to be present at the same harmonics as PE. Applying a bipolar bias causes JH to occur at the zero and second harmonics and PE to occur only at the first harmonic. Applying a bipolar bias allows for independent observation of Joule and Peltier effects as the temperature rise due to Joule heating is at a different harmonic than the temperature rise due to Peltier effects.

Figure 2 shows the predicted device temperature rise at each harmonic due to unipolar and bipolar biases for different values of device thermopower. The zero, first, and second harmonic temperature rises are given by $\Delta T_{0\omega}$, $\Delta T_{1\omega}$, and $\Delta T_{2\omega}$, and the phase of the first harmonic temperature rise is given by $\Theta_{1\omega}$. SJEM cannot measure the non-periodic $\Delta T_{0\omega}$. Also, the maximum voltage applied by the unipolar and bipolar biases is equal, such that the temperature rise of the device due to unipolar and bipolar biases was equal. Therefore, $V_{0\omega}$ and $V_{1\omega}$ under unipolar bias were simulated as one-half of $V_{1\omega}$ under bipolar bias.

Figures 2(a) and 2(b) show the predicted $\Delta T_{0\omega}$ due to unipolar and bipolar biases. Joule heating is evident for both unipolar and bipolar biases as the large and symmetric temperature rise across the channel. Figure 2(a) shows that $\Delta T_{0\omega}$ changes at the contacts with carrier flow direction, indicating local Peltier heating and cooling.[9,10,14] Also, the simulated $V_{1\omega}$ is larger under bipolar bias than unipolar bias which causes a larger predicted $\Delta T_{0\omega}$ for the bipolar bias than the unipolar bias.

Figures 2(c)–2(f) show the predicted peak-to-peak first harmonic temperature rise $\Delta T_{1\omega}$ and phase $\Theta_{1\omega}$ due to unipolar and bipolar biases. Figure 2(c) shows Joule heating, as

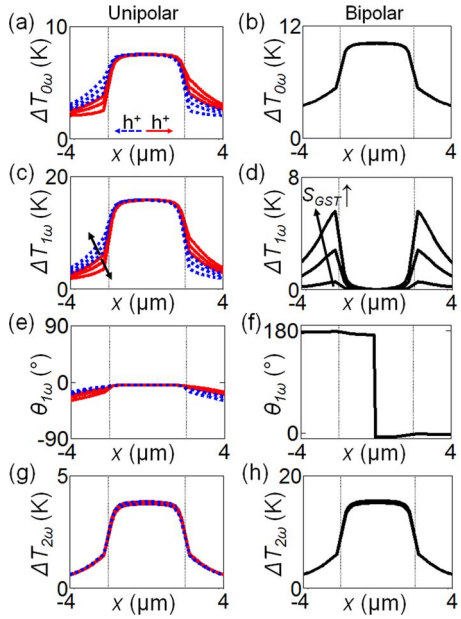

FIG. 2. Predicted harmonic temperature rise due to unipolar and bipolar biases for different values of S_{GST}. (a) and (b) The temperature rise at the zero harmonic $\Delta T_{0\omega}$. (c) and (d) The peak-to-peak temperature rise at the first harmonic $\Delta T_{1\omega}$. Arrows show the direction of increasing S_{GST}. (e) and (f) The phase of the temperature rise at the first harmonic $\Theta_{1\omega}$. (g) and (h) The peak-to-peak temperature rise at the second harmonic $\Delta T_{2\omega}$. The solid red and dashed blue lines show ΔT due to carrier flow to the right and left. The large symmetric ΔT of the channel is due to JH and the change in ΔT with carrier flow at the contacts is due to PE. Vertical dashed lines show the channel edge.

the large temperature rise across the channel, and Peltier effects, as the change in temperature at the contacts with carrier flow direction. Applying a unipolar bias causes both Joule and Peltier effects to be observed in $\Delta T_{1\omega}$. Figure 2(d) shows two positive spikes in $\Delta T_{1\omega}$ at the contacts, which is due to Peltier heating and cooling of the contacts. The predicted $\Delta T_{1\omega}$ is positive for both Peltier heating and cooling as $\Delta T_{1\omega}$ shows only the magnitude of the first harmonic temperature rise. Figure 2(f) shows the predicted $\Theta_{1\omega}$ changes 180° between the contacts indicating the contacts oppositely experience heating and cooling. The 180° shift in $\Theta_{1\omega}$ is further evidence of Peltier heating and cooling of the contacts.[9,10,14] The combination of the observed spikes in $\Delta T_{1\omega}$ and 180 ° shifts in $\Theta_{1\omega}$ indicate a bipolar heated device is experiencing Peltier effects. Figs. 2(d) and 2(f) show only the Peltier effect is observed in the first harmonic temperature rise when applying a bipolar bias.[12] Figure 2(c) shows that increasing the device thermopower increases the change in temperature at the contacts with carrier flow direction, and Fig. 2(d) shows that increasing the device thermopower increases the magnitude of the spikes at the contacts. The changes in Figs. 2(c) and 2(d) at the contacts with increasing thermopower are due to increasing Peltier effects, and fitting FEA predictions to SJEM measurements at the contacts can predict both Peltier effects in the device and the device thermopower.[9,10,12]

Figures 2(g) and 2(h) show the predicted peak-to-peak second harmonic temperature rise $\Delta T_{2\omega}$ due to unipolar and bipolar biases. Joule heating is evident for both unipolar and bipolar biases as the large and symmetric temperature rise across the channel. The simulated $V_{1\omega}$ is larger under bipolar bias than unipolar bias which causes a larger predicted $\Delta T_{2\omega}$ for the bipolar bias than the unipolar bias. Figs. 2(g) and 2(h) show a slight change in $\Delta T_{2\omega}$ with thermopower which is due to the Seebeck effect. The Seebeck effect is described in the supplementary material.[13] Figure 2 shows the predicted harmonic temperature rise of a device due to Joule and Peltier effects and shows that a bipolar bias separates the temperature rise of the device due to Joule and Peltier effects at two different harmonics.

III. APPLICATION TO PHASE CHANGE MEMORY DEVICES

We now show how fitting FEA predictions to SJEM measurements can predict the thermopower of PCM devices, where both Joule and Peltier effects are important.[15] SJEM measurements using both unipolar and bipolar bias investigated JH and PE in lateral $Ge_2Sb_2Te_5$ (GST) devices. We demonstrate that applying a bipolar bias enables independent observation of Joule and Peltier effects in PCM devices and improves the precision of predicting device thermopower.

Figure 3(a) shows a schematic of the lateral GST devices and the SJEM technique. The devices are similar to the model shown in Fig. 1(a), and the geometry and properties of the FEA model were adjusted to match the measured device.[12] Lateral GST devices consisted of 60–110 nm of PMMA, 60 nm of Au, 10 nm TiW, 22 nm GST, and 300 nm SiO_2 on a Si substrate. The device shown in Fig. 3 was annealed at 150 °C for 10 min and has a channel length of 3.6 μm. The measurements shown in Fig. 3 are an average of 32 line scans, and the GST properties were found by fitting the FEA model to each line scan. The first and second harmonic peak-to-peak surface expansions $\Delta h_{1\omega}$ and $\Delta h_{2\omega}$ were measured using

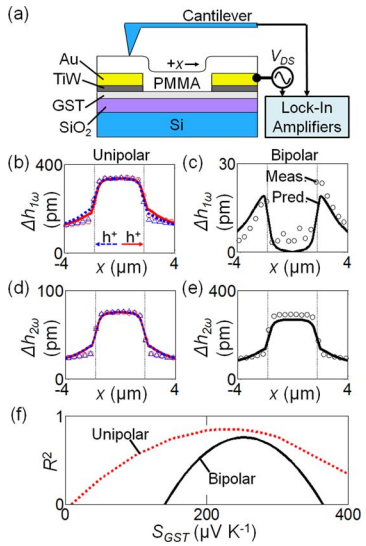

FIG. 3. (a) Schematic of lateral GST devices and scanning Joule expansion microscopy (SJEM) measurements.[13] (b)–(e) Measured and predicted $\Delta h_{1\omega}$ and $\Delta h_{2\omega}$ due to unipolar and bipolar biases. Symbols and solid lines show measurements and predictions. The solid red line and red circles and the dashed blue line and blue triangles show Δh with carrier flow to the right and left. (f) The coefficient of determination R^2 for FEA fitting of SJEM measurements to predict S_{GST}. The bipolar measurement provides significantly improved estimate for S_{GST}.

SJEM and are proportional to $\Delta T_{1\omega}$ and $\Delta T_{2\omega}$. The supplementary material further describes the SJEM measurement.[13]

Figures 3(b) and 3(c) show the measured and predicted first harmonic surface expansion due to unipolar and bipolar biases. Figure 3(b) shows PE cause ~18 pm change in $\Delta h_{1\omega}$ at the contacts with change in bias polarity. The PE is difficult to observe because the $\Delta h_{1\omega}$ due to JH is relatively large. Figure 3(c) shows ~18 pm tall spikes in $\Delta h_{1\omega}$ at the contacts due to PE. The magnitude of the observed PE is the same in Figs. 3(b) and 3(c). However, the $V_{1\omega}$ under unipolar bias was equal to one-half of $V_{1\omega}$ under bipolar bias, and Peltier effects at 1ω scale with $V_{1\omega}$, as shown in Table I. The PE is resolved with two measurements using unipolar heating, while only a single measurement is required using bipolar heating. Since each unipolar heating measurement observes half the PE, the combination of two unipolar measurements yields the same result as a single bipolar measurement.

Figures 3(d) and 3(e) show the measured and predicted second harmonic surface expansion due to unipolar and bipolar biases. Fitting measurements and predictions for $\Delta h_{2\omega}$ yields the GST resistivity $\rho_{GST} = 2.6 \times 10^{-4}$ Ωm and GST-TiW contact resistivity $\rho_C = 2 \times 10^{-9}$ Ωm. The device was biased at $V_{DS} = 2.5$, 3.6, and 4.3 V and all bias conditions were used to fit measurements and predictions. The measurements and predictions are similar for all biases, and only $V_{DS} = 4.3$ V is shown in Figs. 3(b)–3(e) for clarity.

Applying a bipolar bias significantly improves the precision of device thermopower measurements compared to measurements using a unipolar bias. Figure 3(f) shows the error for fitting FEA predictions to SJEM measurements to predict the GST thermopower S_{GST} for unipolar and bipolar based measurements. The coefficient of determination R^2 is the error between predictions and measurements for predicting ρ_{GST}, ρ_C, and S_{GST}. Figure 3(b) shows the Peltier effect causes a difference in $\Delta h_{1\omega}$ with carrier flow direction. Fitting FEA predictions to SJEM measurements of the difference in $\Delta h_{1\omega}$ with carrier flow direction predicts $S_{GST} = 240 \pm 26$ μV K^{-1}.[9,10] Fitting the measured and predicted $\Delta h_{1\omega}$ using the bipolar technique predicts $S_{GST} = 250 \pm 10$ μV K^{-1}. The S_{GST} predicted using a bipolar bias has a smaller deviation than the S_{GST} predicted using a unipolar bias. The average measured uncertainty of $\Delta h_{1\omega}$ for measurements using unipolar and bipolar biases are ~8 and ~2 pm. The measurement uncertainty of the unipolar measurements is larger than that of the bipolar measurements for observing Peltier effects, which increases the predicted uncertainty of thermopower measurements when using a unipolar bias. The supplementary material describes the measurement uncertainty.[13]

Measurements using a bipolar bias to independently observe JH and PE have several advantages over measurements using a unipolar bias. Measurements using a bipolar bias have lower measured uncertainty for observing PE than measurements using a unipolar bias,[13] which increases the precision of thermopower measurements and allows for observation of thermoelectric effects in low thermopower devices. Bipolar heating also enables lateral mapping of devices with heterogeneous Joule and thermoelectric effects,[12] since the thermoelectric effects can be resolved with a single measurement;

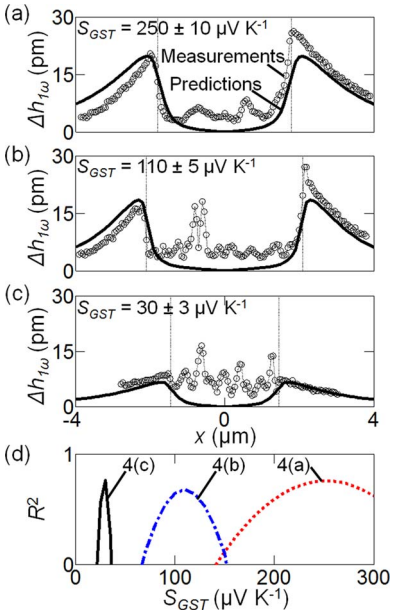

FIG. 4. Measured and predicted $\Delta h_{1\omega}$ from a bipolar bias for three GST devices with predicted $S_{GST} = 250 \pm 10$ (a), 110 ± 5 (b), and 30 ± 3 (c). (d) The error of the predicted S_{GST} from FEA fitting to SJEM measurements for the three devices. Fitting FEA predictions to SJEM measurements for bipolar heating enables precise prediction of material thermopower from 30 to 250 μV K^{-1}. The additional measured $\Delta h_{1\omega}$ peaks shown in the channel of 4(b) and 4(c) are due to PE between GST phases.[12]

unipolar measurements require two precisely aligned measurements to resolve nanometer-scale thermoelectric effects. Finally, measurements using a bipolar bias can be performed twice as fast as a unipolar measurement.

We now investigate the measurement sensitivity of the bipolar bias technique by observing thermoelectric effects in devices with lower thermopowers. Figures 4(a)–4(c) show the measured and predicted $\Delta h_{1\omega}$ for three GST devices with different properties. Figure 4(a) shows the measured and predicted $\Delta h_{1\omega}$ from the device shown in Fig. 3. Figures 4(b) and 4(c) show devices with channel lengths of 4.2 and 2.9 μm which were annealed at temperatures of 200 and 250 °C for 10 min. Figure 4(d) shows the error for fitting FEA predictions to SJEM measurements to predict S_{GST} for the three devices. Figure 4(d) shows that measurements using a bipolar bias enable precise prediction of material thermopower from 30 ± 3 to 250 ± 10 μV K^{-1}. The supplementary material describes the predicted uncertainty of S_{GST} between the three devices.[13] Figure 4(c) shows good agreement between measurements and predictions and indicates that measurements using a bipolar bias enable accurate prediction of the material thermopower down to ~30 μV K^{-1}, the lowest thermopower device available for this study.

IV. CONCLUSION

In conclusion, we developed a technique for independent observation of nanometer-scale Joule and thermoelectric effects, using AFM based measurements of nanometer-scale temperature fields. The temperature rise of a device is governed by both Joule and thermoelectric effects, and heating a

device with a periodic and bipolar bias separates the temperature rise due to Joule and thermoelectric effects at different harmonics. An AFM based thermometry technique known as SJEM can simultaneously observe both the Joule and Peltier harmonic temperature rise of the device, such that Joule and Peltier effects can be independently observed. The independent observation of nanometer-scale Joule and thermoelectric effects improves the sensitivity and precision of nanometer-scale thermoelectric measurements. We couple predictions and measurements of the temperature rise of PCM devices for precise prediction of device thermopower from 30 ± 3 to 250 ± 10 μV K^{-1}. Furthermore, the derived harmonic relations for Joule and thermoelectric effects are applicable to other thermometry techniques; facilitating new studies of nanometer-scale Joule and thermoelectric heating, vital to the design of efficient electronics.

ACKNOWLEDGMENTS

The authors gratefully acknowledge the help of S. Somnath and J. P. Llinas and support by the National Science Foundation (NSF) grant ECCS 10-02026 and by the Materials Structures and Devices (MSD) Focus Center, under the Focus Center Research Program (FCRP), a Semiconductor Research Corporation entity.

[1]E. Pop, Nano Res. **3**, 147 (2010).
[2]A. Jungen, M. Pfenninger, M. Tonteling, C. Stampfer, and C. Hierold, J. Micromech. Microeng. **16**, 1633 (2006).
[3]G. Bakan, N. Khan, H. Silva, and A. Gokirmak, Sci. Rep. **3**, 2724 (2013).
[4]J. Park, G. He, R. M. Feenstra, and A.-P. Li, Nano Lett. **13**, 3269 (2013).
[5]J. C. Walrath, Y. H. Lin, K. P. Pipe, and R. S. Goldman, Appl. Phys. Lett. **103**, 212101 (2013).
[6]K. Kim, W. Jeong, W. Lee, and P. Reddy, ACS Nano **6**, 4248 (2012).
[7]B. Desiatov, I. Goykhman, and U. Levy, Nano Lett. **14**, 648 (2014).
[8]J. Varesi and A. Majumdar, Appl. Phys. Lett. **72**, 37 (1998).
[9]K. L. Grosse, M.-H. Bae, F. Lian, E. Pop, and W. P. King, Nat. Nanotech. **6**, 287 (2011).
[10]K. L. Grosse, F. Xiong, S. Hong, W. P. King, and E. Pop, Appl. Phys. Lett. **102**, 193503 (2013).
[11]X. Xie, K. L. Grosse, J. Song, C. Lu, S. Dunham, F. Du, A. E. Islam, Y. Li, Y. Zhang, E. Pop, Y. Huang, W. P. King, and J. A. Rogers, ACS Nano **6**, 10267 (2012).
[12]B. Bhatia, "Nanometer-Thick Oxide Films for Pyroelectric Energy Conversion," Ph.D. Dissertation, University of Illinois, 2014.
[13]See supplementary material at http://dx.doi.org/10.1063/1.4895715 for details of the FEA model, the Seebeck effect, the SJEM measurements, and the measurement uncertainty.
[14]F. J. DiSalvo, Science **285**, 703 (1999).
[15]J. Lee, M. Asheghi, and K. E. Goodson, Nanotechnology **23**, 205201 (2012).